Journal of Atmospheric and Solar-Terrestrial Physics 189 (2019) 65–79

Contents lists available at ScienceDirect

Journal of Atmospheric and Solar-Terrestrial Physics

journal homepage: www.elsevier.com/locate/jastp

Multi-instrument investigation of troposphere-ionosphere coupling and the role of gravity waves in the formation of equatorial plasma bubble

M. Sivakandan[a,*], I. Paulino[b], T.K. Ramkumar[c], A. Taori[d], A.K. Patra[c], S. Sripathi[e], K. Niranjan[f], A.V. Bilibio[g]

[a] Physical Research Laboratory, Ahmedabad, 380009, India
[b] Universidade Federal de Campina Grande (UFCG), Campina Grande, Brazil
[c] National Atmospheric Research Laboratory, Gadanki, 517112, India
[d] Regional Remote Sensing Center (RRSC), Nagpur, India
[e] Indian Institute of Geomagnetism, Navi Mumbai, 410218, India
[f] Department of Physics, Andhra University, Visakhapatnam, 530003, India
[g] Instituto Nacional de Pesquisas Espaciais (INPE), São José dos Campos, Brazil

ARTICLE INFO

Keywords:
Equatorial plasma bubbles
R-T instability
Gravity waves
Ray tracing

ABSTRACT

Present study investigates the role of gravity waves in the generation of equatorial plasma bubbles (EPBs) during geomagnetic quiet conditions using co-located observations from Gadanki (13.5°N, 79.2° E) an all sky airglow imager, Gadanki Ionospheric Radar Interferometer (GIRI) and Ionosonde observations from Tirunelveli (8.7° N, 77.8° E). To avoid any changes occurring in the background ionosphere, four consecutive nights of observation during 03–06 February 2014 is used. Out of these four nights, three nights (i.e., 03, 05 and 06 February 2014) exhibit occurrence of EPBs in the OI 630 nm airglow emission and radar plumes and there is no bubble occurrence during one night, though the ionospheric peak altitude (h′F) value is more than 350 km in all these nights. During these four nights the structures observed in the E-region drifts and gravity waves noted in the mesospheric OH emissions are analyzed. It is found that there are common periodic oscillations in the OH peak emission altitude and E-region in three nights (03, 04 and 05 February 2014). The mesospheric gravity wave structures are ray traced to their potential sources in the lower atmosphere and also for the possibility of their propagation to the E-region. Our results suggest that apart from horizontal wavelength and amplitudes, the propagation angle of gravity wave may also be important for seeding of the Rayleigh-Taylor (R-T) instability. Thus, it gives an insight about the role of lower – middle and upper atmospheric coupling on the occurrence of the noted EPBs.

1. Introduction

Even after the last few decades of investigation on the causative mechanisms of the equatorial plasma bubbles (EPBs)/Spread-F, it remains an enigma in the equatorial ionospheric dynamics. Understanding and predicting the occurrence of EPB is not limited to academic interest, but also of practical relevance with regards to satellite based communication/navigation applications. EPB is primarily governed by the Rayleigh-Taylor (R-T) instability initiated at the bottom side of the F-region. The R-T instability was first proposed by Dungey (1956). The growth rate of R-T instability in collision dominated plasma is,

$$\gamma_{RT} = \frac{g}{\upsilon_{in}} . \frac{1}{n} \nabla n \tag{1}$$

where, g is the acceleration due to gravity, υ_{in} is the ion-neutral collision frequency, n is the background electron density and $\nabla n = \frac{\partial n}{\partial h}$ is the vertical electron density gradient.

Equation (1) suggests that a high growth rate is expected when υ_{in} is small and ∇n is high. This implies that the height of the F-layer base should be high and the bottom side should provide sharp density gradient. Both conditions are often satisfied after the sunset when the recombination eats away the bottom side F-layer and large eastward electric field which an equatorial phenomena known as Pre-Reversal Enhancement (PRE) whereby the F-layer is pushed to the higher heights.

* Corresponding author.
E-mail addresses: skandanm89@gmail.com, sivakandan@prl.res.in (M. Sivakandan).

https://doi.org/10.1016/j.jastp.2019.04.006
Received 19 November 2018; Received in revised form 4 April 2019; Accepted 5 April 2019
Available online 10 April 2019
1364-6826/

A quasi-sinusoidal perturbation is also required for the R-T instability to grow (e.g., Kelley et al., 1981). To investigate the EPB characteristics, ground based [e.g., radar, airglow photometer, airglow imager, Ionosonde (e.g., Kelley et al., 1981; McClure et al., 1977; Mendillo et al., 1992; Taori et al., 2010; Taori and Sindhya, 2014; Weber et al., 1978)], space borne (Costa and Kelley, 1978) measurements have been extensively carried out. Tsunoda (1985) showed that when the sunset is simultaneous at the conjugate E−regions, the eastward polarization electric field contributes to the enhancement of irregularity production via the generalized gradient drift instability. Further, Mendillo et al. (1992) pointed out that post sunset F-region rise and the availability of a seed perturbation are the pre-requisites for R-T instability growth. In addition to the above, the investigations using the Jicamarca radar suggested the R-T instability seeding by gravity waves (e.g., Kelley et al., 1981; Hysell et al., 1990). Since then there are several studies which have supported the gravity wave seeding theory (e.g., Prakash and Pandey, 1985; Taori et al., 2011a,b). For example, Singh et al. (1997) suggested that gravity waves in the environment probably caused the wave like ion-density structures and hence provided the initial seed ion density perturbations. By using lidar, MST radar and ionosonde data Taori et al. (2012) reported the linkage between the gravity waves and EPB occurrences during low solar activity over the Indian sector.

Further, using multiple instruments in SpreadFEx campaign, it is reported that there is a direct link between deep tropical convection and large gravity wave perturbations at large spatial scales (at the bottom side F layer). Reports also show their likely contributions to the excitation of R-T instability and plasma bubbles extending to much higher altitudes over the Brazilian sector (Fritts et al., 2009; Vadas et al., 2009, and reference therein). Takahashi et al. (2009) showed a linear relationship between the gravity wave wavelengths and the distances between plasma bubble structures using airglow measurements over the Northeast of Brazil. Later, Paulino et al. (2011) found similar result using the airglow observations in the northern part of Brazil.

Over the Indian sector, using simultaneous airglow and radar observations, it was shown that there is a linkage between mesospheric gravity wave and EPB structures (Taori et al., 2012) and that there is a quasi-sinusoidal feature in the F-region before the occurrence of EPBs (Patra et al., 2013). The present study extends Taori et al. (2012) study using different dataset along with ray-tracing techniques to fill the gap between the wave sources and E-region (based on the mesospheric wave signatures noted in mesospheric altitudes). We collected simultaneous data (using airglow imager, 30 MHz radar and ionosonde) during 03–06 February 2014 (quiet geomagnetic conditions) when a variety of EPBs and mesospheric waves were noted. Therefore, we separated the data in three categories: 1) Occurrence of EPBs with mesospheric gravity waves, 2) Identifiable mesospheric gravity waves with no EPB occurrence, and 3) Occurrence of EPBs without mesospheric gravity waves. Together with these data, we also used ray tracing technique to complement our results. In this paper, instrumentation and data analysis are presented in section 2, results and discussion are given in section 3 and 4, and summary and conclusions are presented in section 5.

2. Instrumentation and data analysis

To understand the seeding of EPBs/ESF and atmospheric coupling processes, we used multiple instruments such as All sky airglow imager Gadanki Ionospheric Radar Interferometer (GIRI) over Gadanki and ionosonde at Tirunelveli. Details of these instruments are given below.

2.1. All sky airglow imager

An all sky airglow imager is installed and being operational in moonless (± 6 days from the new moon) and cloud free (clear sky) nights at National Atmospheric Research Laboratory (NARL), Gadanki (13.5^0 N, 79.2^0 E, 6.51 dip lat.,) since 16 March 2012. NARL airglow imager (NAI) consists of a fish eye lens, filter chamber, paralleling lens, filter chamber temperature controlling unit, charge coupled device (CCD-ActionPixis1024B) of size 13.3 μm with 100% fill factor and 16-bit depth, and an imager controlling system. At operational condition the CCD is maintained at −70 °C temperature by thermoelectric temperature controller (in order to reduce the thermal noise). To increase the signal-to-noise ratio (SNR) (i.e., to decrease the readout noise), the images are binned for 2 × 2 pixel on the chip making an effective 512 × 512 super pixel image. To monitor the various airglow emission intensities, the filter chamber contains three different filters viz., a wide band filter for OH (720–900 nm and notched at 865 nm; peak altitude ~85 km) measurements, and two narrow band filters with full width half maximum (FWHM) of 2 nm for OI 557.7 nm (peaks altitude ~96 km) and for OI 630 nm (peak altitude ~250 km) measurements (Khomich et al., 2008). The full field of view (FOV) of the imager is 180° degrees, however due to the walls of the observational dome, at present the effective FOV is ~117°. With the present FOV (~117°), the images cover an area of ~600 × 600 km [corresponding latitude and longitude ~10.5–16.5° N; 76–82°E; ~3.3–10° magnetic latitude) at the OI 630 nm peak emission altitude of 250 km. Further description about NAI, its data analysis and first results are available in Taori et al. (2013). In the present study, OH and OI 630 nm images are used to understand the mesosphere-thermosphere coupling processes.

The acquired raw images are unwrapped and projected onto an equidistant grid, prior to extraction of the wave parameters from the OH images and plasma parameters from the OI 630 nm images. Median filter method is used to remove the stars in the images. The atomic oxygen red line emission is generated by the transitions from the O (^{1}D) metastable state. The mechanism of the excitation of metastable oxygen atoms at night in geomagnetic quiet conditions is related to the dissociative recombination processes (Khomich et al., 2008) ($O^+ + O_2 \rightarrow O_2^+ + O$ $O_2^+ + e \rightarrow O + O^1D$)). The emission rate is depending on the electron concertation and molecular oxygen. Thus, it represents the electron density variation in the bottom side ionosphere. The radiative life time of oxygen red line emission is ~110 s (Brasseur and Solomon, 2005).

Fig. 1 shows samples of OI 630 nm raw image (Fig. 1a) and processed image (Fig. 1b) respectively. In Fig. 1b, X-and Y-axis indicates image covering area in zonal (East-West) and meridional (North-South) direction around OI 630 nm emission altitude (i.e. ~250 km). Centre of these images denote the observational location (i.e. Gadanki). The centre is located at the intersection of vertical and horizontal dashed yellow lines that is marked at 0 km (location of Gadanki). Northward and eastward directions are considered positive in the image. Red dotted arrow represents the plasma bubbles drift towards east direction. The image data obtained from Gadanki are further analyzed to construct East-West (EW) keograms (fixed latitude with varying longitudes) and North-South (NS) keograms (fixed longitude with varying latitudes). The part of the image enclosed by the red dashed lines (Fig. 1b) is used to construct the keograms (averaged over 3 pixels).

2.2. Gadanki Ionospheric Radar Interferometer (GIRI)

The operating frequency of GIRI is 30 MHz and it consists of a rectangular antenna array of 160 (20 × 8) two-element Yagi antenna, 20 transmitter units providing a maximum peak power of 160 kW, six digital receivers including data processing systems, a radar controller, and a host computer. The antennas are separated by 0.56λ (5.6 m) in east-west and 0.7λ (7 m) in north-south directions, where λ (= 10 m) is the radar wavelength. The antenna elements are physically oriented at an angle of 14° from horizontal to make them nearly parallel to Earth's magnetic field. While forming the radar beam transverse to the magnetic field, which is required for detecting the backscatter from field aligned irregularities (FAI), this arrangement maintains the antenna

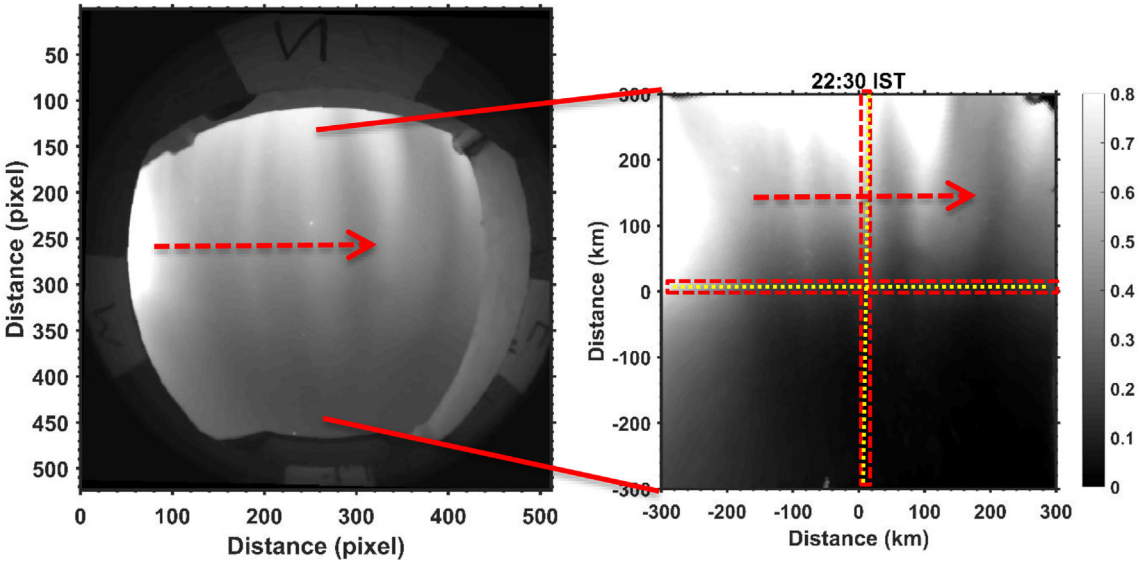

Fig. 1. Sample images of OI63nm emission: a) raw image and, b) processed image (22:30 IST) on 03 February 2014, centre of these images implies the observational location (i.e. Gadanki). In Fig. 1a and b, X-and Y-axis denotes image covering area (in pixels and in km) in zonal (East-West) and meridional (North-South) direction around OI630nm emission altitude (i.e. ~250 km). The centre is located at the intersection of vertical and horizontal dashed yellow lines that are marked at 0 km, and red dashed rectangle region implies the portion that is taken for east west and north south keogram. In these figures, red dashed arrow implies the north-south aligned eastward moving EPB signature.

gain at its peak at 14° off-zenith direction. The half-power full width of GIRI is 4.5° in the east-west and 9° in the north-south planes. Each transmitter receiver (TR) module feeds a north-south-aligned linear array of eight antennas through a fixed phase-shifting network. The antenna array is phased in the east-west direction, and beam can be formed in any direction up to ± 50° (azimuth angles 310°–50°) with respect to the direction perpendicular to the Earth's magnetic field. Similarly, the beam can be changed on a pulse-to-pulse basis to perform fast beam scanning. Further, detailed descriptions of GIRI and its first results are available in Patra et al. (2014).

2.3. Ionosonde

In the present study, we use Canadian Advanced Digital Ionosonde (CADI) which is located at Tirunelveli (8.7° N, 77.8° E, dip 0.15° N). The CADI consists of a transmitter which is capable of operating in the frequency range of 1–20 MHz, four receivers, and two sets of antenna system. The transmitter peak power is 600 W. The transmitter antenna is a delta antenna, and the receiver antenna array consists of four dipoles arranged in the form of a square. The Pulse Repetition Frequency (PRF) of 20 Hz and pulse width of 40 μs is used to get ionograms with a sampling interval of 100 kHz providing a height resolution of 3 km. It uses 13-bit barker code to get better signal to noise ratio with good height resolution (~3 km) (Huang and MacDougall, 2005).

2.4. Ray tracing method

If a gravity wave packet is propagating in a fluid, with background wind $\vec{V}(\vec{x}) = (u, v, w)$, its temporal and spatial evolution can be described by Lighthill (1978):

$$\frac{dx_i}{dt} = V_i + \frac{\partial \omega_{Ir}}{\partial k_i} = V_i + c_{gi} \tag{2}$$

and

$$\frac{dk_i}{dt} = -k_j \frac{\partial V_j}{\partial x_i} - \frac{\partial \omega_{Ir}}{\partial x_i} \tag{3}$$

where $\omega_{Ir} = \omega_{Or} - \vec{k}.\vec{V}$ is the intrinsic frequency of the gravity waves, ω_{Or} is the observed frequency, $\vec{k}$ is the wave vector in a given time, $\vec{x}$ is the position of the wave at a given time, c_{gi} is the group velocity, $i, j = 1,2,3$ and repeated indices imply a summation.

By solving this equation system, it is possible to follow the path of the gravity waves into the atmosphere. The main challenge for ray-tracing of gravity waves is to know the wind and temperature, i.e., the thermodynamics in the whole atmosphere.

The initial conditions used to solve the set of equations assume the position of the observatory and the airglow layer height, i.e., $\vec{x}(t=0) = (x, y, z) = (79.2^oE,\ 13.5^oN,\ 85\ km)$ and the initial wave vector is calculated by $\vec{k}(t=0) = (k, l, m) = \left(\frac{2\pi}{\lambda_x}, \frac{2\pi}{\lambda_y}, m\right)$, where $K_H = \sqrt{\left(\frac{2\pi}{\lambda_x}\right)^2 + \left(\frac{2\pi}{\lambda_y}\right)^2}$ is the horizontal wave number.

The horizontal wave number is calculated using the horizontal wavelength of the gravity wave estimated from the OH airglow images and the vertical wave number is derived using the Marks and Eckermann (1995) dispersion relation

$$m^2 = \frac{(k^2 + l^2)N^2}{\omega_{Ir}^2} - (k^2 + l^2) - \frac{1}{4H^2} \tag{4}$$

where N is the buoyancy frequency and H is the scale height.

The wind and temperature inputs to the ray tracing model are based on the Horizontal Wind Model (HWM-07; Drob et al., 2008) and Naval Research Laboratory Mass Spectrometer and Incoherent Scatter Radar model (NRLMSISE-00; Picone et al., 2002), respectively (Vadas and Fritts, 2009). In order to estimate the effect of the wind in the ray path of the gravity waves, comparison between HWM background wind and zero wind are carried out.

Moreover, the thermal diffusivity and molecular viscosity (in the thermosphere) which dissipates the gravity waves, must be considered into the ray tracing equations. The dispersion relation, (used in this study the dissipative effects) becomes complex. Its real part, which is presented in Equation (26) of Vadas and Fritts (2005), gives the propagation condition into the thermosphere and its imaginary part (Equation 25 of Vadas and Fritts, 2005) gives the inverse decay rate along the time. Since the imaginary part of the dispersion relation changes in time and space, the spectral momentum flux per unit of mass are estimated based on Equation (50) of Vadas and Fritts (2009). In the context of effect of winds on gravity wave upward propagation, please

note the work by Yiğit et al. (2008), which considered in detail the effect of windless atmosphere versus an atmosphere with wind. This work outlines how the winds can affect the upward propagation of gravity waves, taking into account various physics-based dissipation processes suitable for the thermosphere, including nonlinear interactions between individual waves. Also, note that ion drag dissipation of gravity waves is an additional physical processes that should be kept in mind (Medvedev et al., 2017) at ionospheric altitudes.

The ray tracing path for a given gravity wave starts from the OH layer at 87 km height and goes downward to the ground (reverse ray tracing). Then, the path goes in a direct way up to the complete dissipation of the gravity wave into the thermosphere (forward tracing), which is assumed to be one billion part of the initial amplitude of the gravity waves measured at the OH layer. There are other three stop conditions: (1) if the group speed of the gravity waves becomes 90% of the sound speed; (2) whenever the kinematic viscosity changes quickly or (3) the gravity wave reaches a critical level. Further details about the ray tracing simulation used in this work can be found in Paulino et al. (2012).

3. Results

3.1. F-region plasma depletions/plumes

In present study, multi-instruments (all sky airglow imager, 30 MHz radar and ionosonde) data sets are used for four consecutive quiet geomagnetic nights (Ap index less than 18 - Ap values are given in Table 1) from 03 February 2014 to 06 February 2014, to address the role of gravity waves in generation of equatorial plasma bubbles (EPBs). Out of these four nights, on three nights (03, 05 and 06 February 2014) EPB occurrence is noted while on one night (04 February 2014) no depletion occurred (very weak echoes in 30 MHz). In order to derive the plasma zonal drift and inter-depletion distances, east west (EW) and north-south (NS) keogram is constructed (Fig. 2). In Fig. 2, the right side figures denote the NS keograms and the left side figures denoted the EW keograms where the X-axis represents time (in Indian Standard Time-IST) and Y-axis represents zonal (EW keogram) and meridional (NS keogram) distances. The plasma bubbles are the blue color (low intensity) structure which appears first in the western side and later it drifted towards the eastern side of the EW keograms as indicated by the red arrows and the inter-depletion period can be observed from the NS keograms (indicated by black arrows).

The EPB characteristics such as zonal drift velocity and inter-depletion distance are estimated from the airglow images using the method by Taori and Sindhya (2014). Some of the key points from their method is as follows, the spatial displacement and time difference between successive images provide the equatorial plasma drift (EPD) velocity. The error in estimating the maximum gradient is less than 2 pixels which results in an error of ± 7 m/s. The distance between two successive depletions is referred as inter-depletion distance. Overall, the EPB characteristics and geomagnetic condition during these nights are given in Table 1. On 03 Feb 2014, there is a deep plasma depletion which moves eastward with a drift velocity 163.7 ± 13 m/s and the inter-depletion distance varies from ~110 to 210 km. On 05 Feb 2014, depletion occurrence is weak which also moves to the east direction with a drift velocity of 122.6 ± 11.3 m/s. Two predominant size of inter depletion distances are noted on this night, one is ~55.8 ± 5 km and another one is 376 ± 33 km. Further, on 06 February 2014, a strong EPB event is monitored and depleted structures are found to move in the east direction with drift velocity of 70 ± 9.7 m/s. Strength of the plasma depletion is described by the 30 MHz radar SNR values (shown in Fig. 3) as described in following section.

In order to confirm whether the noted airglow depletions are EPB or only the airglow intensity depletion, a co-located simultaneous back scattered 30 MHz radar range-time- intensity (RTI) maps for above mentioned nights are checked (Fig. 3). It is observed that on all the three nights the depletions started at around 20:00 IST [14:30 Universal Time Coordinate (UTC)]. However, on 05 February 2014 the depletion is getting strengthened around ~21:30 IST (16:00 UTC). In order to calculate the inter depletion period from radar data, the SNR values at around 350 km is taken and using the empirical mode decomposition (EMD) and Lomb Scargle Periodogram (LSP) analysis inter depletion periods are derived that will be discussed in section 3.2.3.

In order to understand the background ionospheric condition i.e., F-layer height variation, vertical drift and zonal electric fields are checked using the Tirunelveli Ionosonde data (it is an equatorial station, located 600 km south of the Gadanki). Fig. 4 show the variations of virtual height of the F-layer, h′F over Tirunelveli. From Fig. 4 it is clear that h′F values exhibit a sudden rise during the post sunset hours (i.e., 18:30–19:30 IST (13:00–14:00 UTC)). On 03 February before the occurrence of spread-F, h′F is raised up to ~400 km, while on 05 February the h′F values reach ~375 km and about 475 km on 06 February before the occurrence of spread-F. The h′F values on 04 February 2014, when no spread-F was observed, is about 410 km. Further, the vertical drift and zonal electric field variations are derived using ionosonde h′F values. The vertical drift goes as high as 65 m/s on 03 February 2014 and remaining nights it goes up to 40 m/s. Earlier reports suggest that when the seed perturbations is omnipresent the threshold height and vertical drift for spread F to occur is 305 km and 23–30 m/s respectively, during the equinoxial months over the Indian sector (Fejer et al., 1999; Jayachandran et al., 1993; Manju et al., 2007). The present h′F value and vertical drifts are above the normal threshold values for spread-F to occur; however, there is no bubble on 04 February 2014.

The results presented above poses more curious questions that what is more important even when the background ionospheric conditions (h′F values exceeds more than 350 km and vertical drift reaches up to 40 m/s) are favorable? It leads us to look for the variability in trigger mechanism, i.e., the seed or a quasi-sinusoidal perturbation under an unstable ionosphere. In order to understand the R-T instability growth from the lower atmospheric forcing, we looked into the role of gravity waves in the mesosphere lower thermosphere (MLT) dynamics using the 30 MHz radar E−region drift velocity and OH airglow emission intensity variations. This will be discussed in the following sections.

3.2. Identification of gravity waves in the MLT region

To identify the common wave period oscillations in the mesosphere, E-region and F-region; the following data processing techniques such as: 1) Empirical mode decomposition (EMD), and Lomb-Scargle Periodogram (LSP) and 2) Keogram analysis are used. A brief description of these techniques are given below.

Table 1
Plasma parameters and Ap index during four consecutive nights.

Sl. No.	Date	Zonal drift velocity (m/s)	Interception Distance (km)	Ap index
1	03-02-2014	163.7 ± 13	110–210	6
2	04-02-2014	NIL	NIL	4
3	05-02-2014	122.6 ± 11	55.8 ± 5; 376 ± 33	3
4	06-02-2014	70 ± 10	–	8

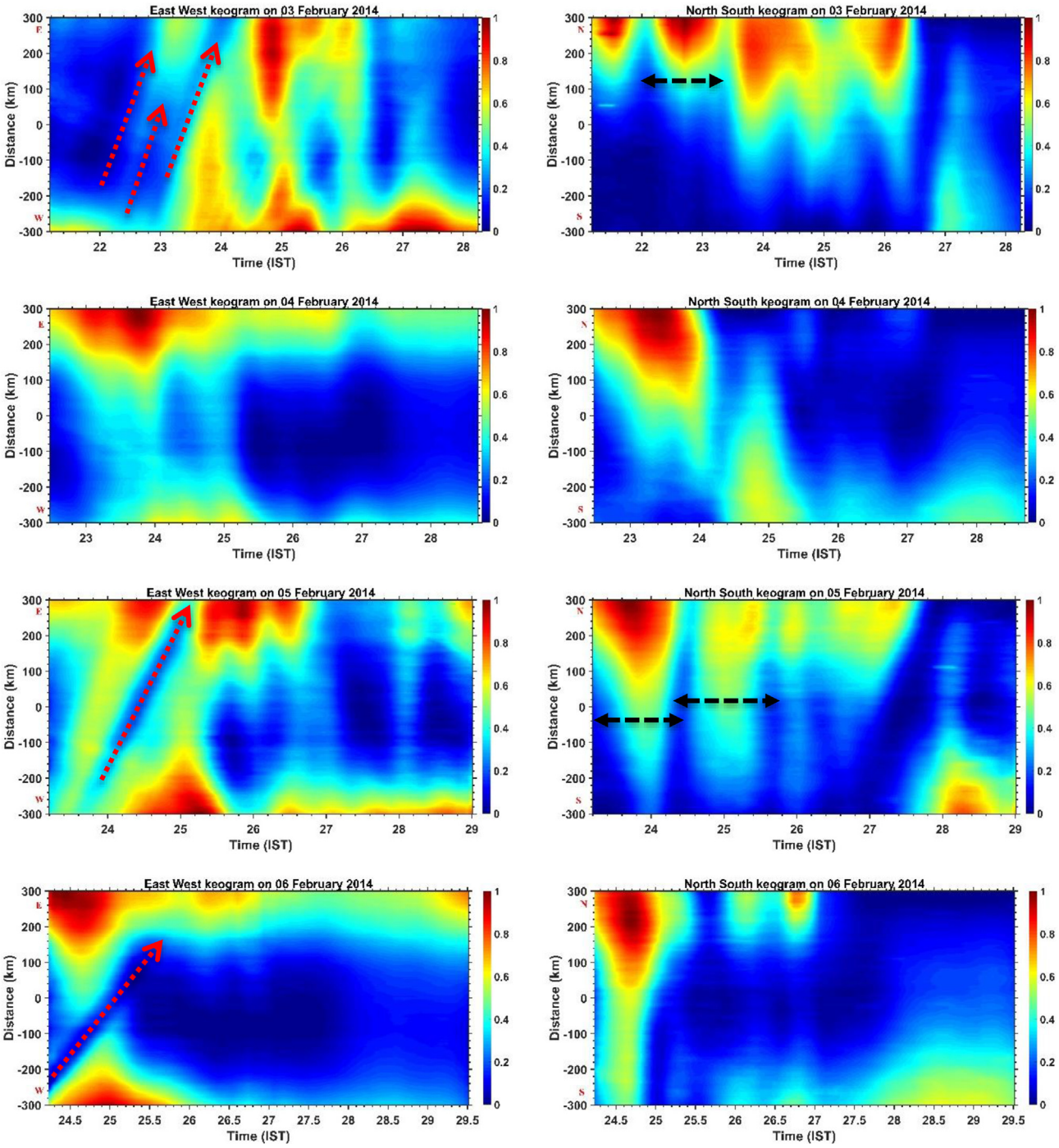

Fig. 2. EW (left side) and NS (right side) Keogram of OI630nm night time airglow emissions for 03–06 February 2014. In these figures, X-axis denotes the time and Y-axis denotes the zonal (EW keogram) and meridional distance (NS keogram). The west to eastward EPB drifts are highlighted by red dotted arrows (see EW keogram) and the inter-depletion periods are indicated by a black dotted arrows (see NS keogram). EW keogram show the signature of EPB during 03, 05 and 06 February 2014, and no EPB on 04 February 2014.

3.2.1. Empirical mode decomposition (EMD) and Lomb Scargle Periodogram (LSP)

To investigate the common wave period in the E (drift velocity) and F (signal to noise ratio-SNR) region, EMD technique is performed for the E-region drift velocity and F-region SNR data. It is an efficient method to analyses the nonlinear and non-stationary data. Using the EMD method, any complicated data set can be decomposed into a finite and often small number of intrinsic mode functions (IMFs) and which leads to a clean representation of the signal by a few well behaved signal components. In this technique, any signal consisting of different IMFs should satisfy the following two assumptions: (1) in the whole data set, the number of extrema and number of zero crossings are either equal or differ at the most by one. (2) At any point, the mean value of the envelope defined by local maxima and the envelope defined by the local minima approach is zero (Huang et al., 1998; Kishore et al., 2012).

The decomposition method can simply use the envelopes defined by the local maxima and minima separately. Once the extrema are identified, all the local maxima are connected by a cubic spline line as the upper envelope. The procedure is repeated for the local minima to produce the lower envelope. These envelopes should cover all the data

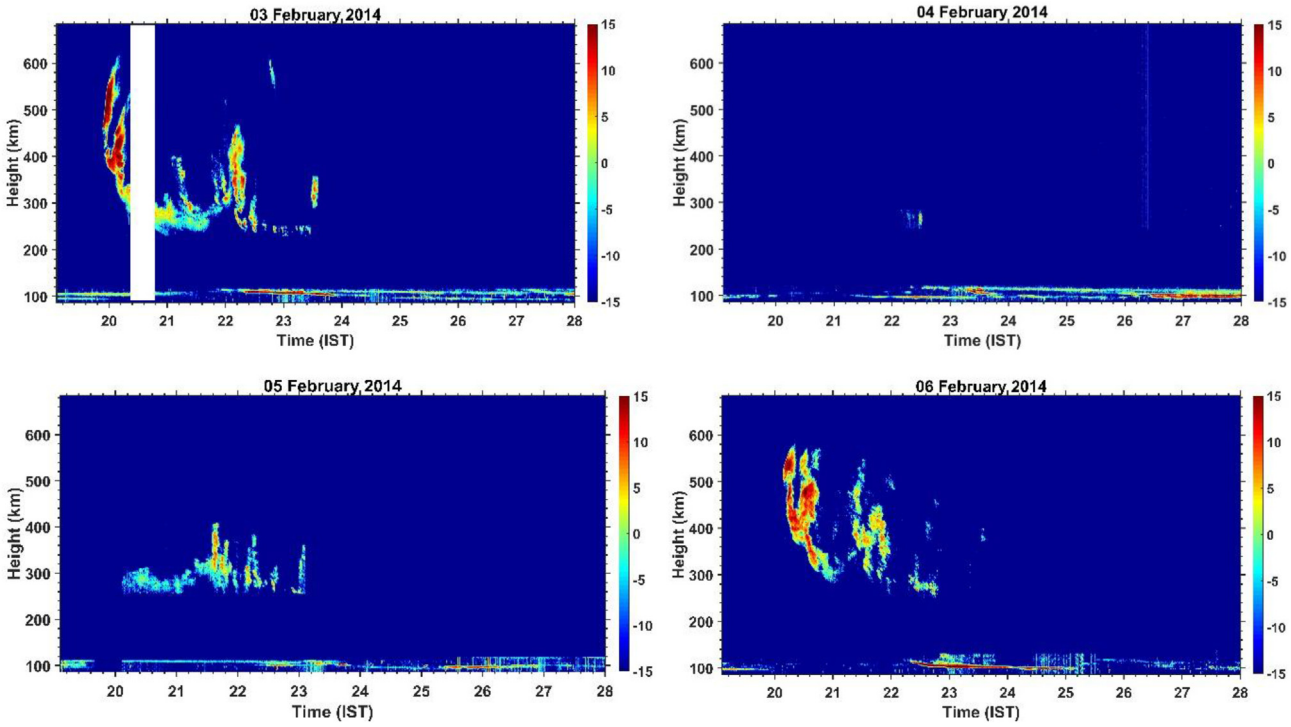

Figure 3. 30 MHz radar backscatter Range-time-intensity (RTI) maps from 03 to 06 February 2014. Except 04 Feb 2014 remaining three days shows the plasma plumes occurrences. On 03 and 06 February 2014, signal to noise ratio (SNR) value shows a well-developed plasma plumes which goes as high as 600 km. Vertical extension of the EPB started at 21:30 IST during 05 February 2014 and its vertical development is small in comparison to the other two nights.

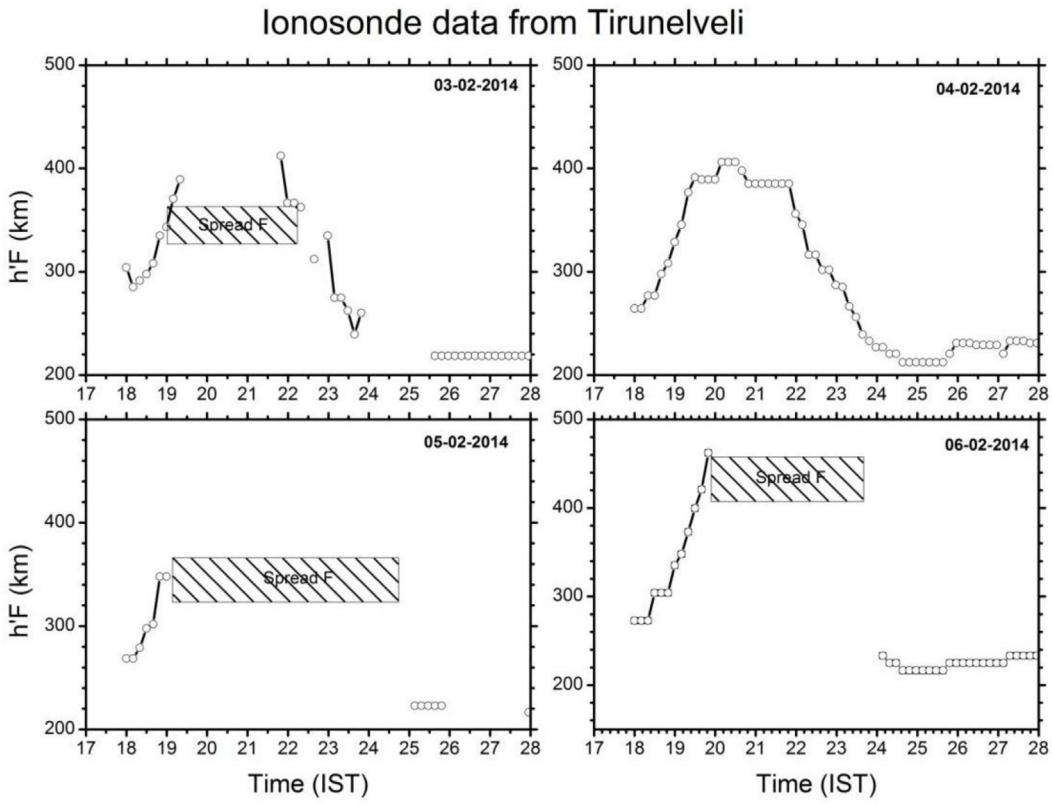

Fig. 4. F-region virtual height (h'F) over Tirunelveli using ionosonde from 03 February 2014 to 06 February 2014. It is evident that during all these nights, h'F value exceeds more than 350 km which is the threshold level for the generation of EPB over the Indian sector.

a) EMD and LSP for OH emission zenith intensity

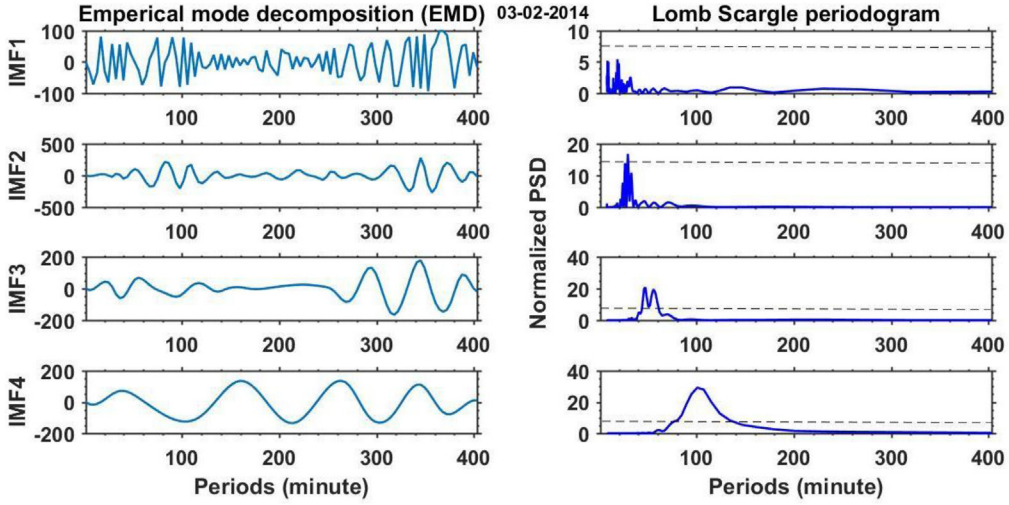

b) EMD and LSP for E region drift velocity

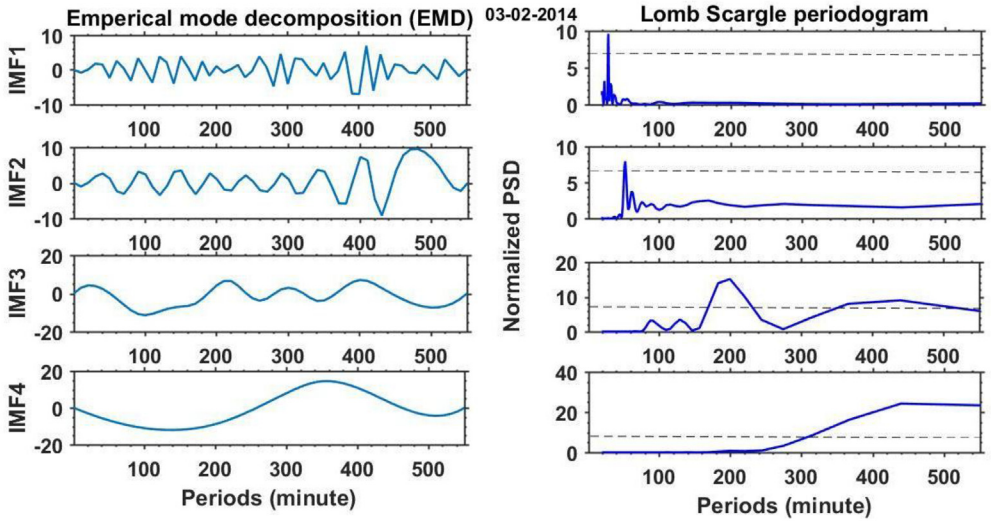

c) EMD and LSP for 350 km SNR.

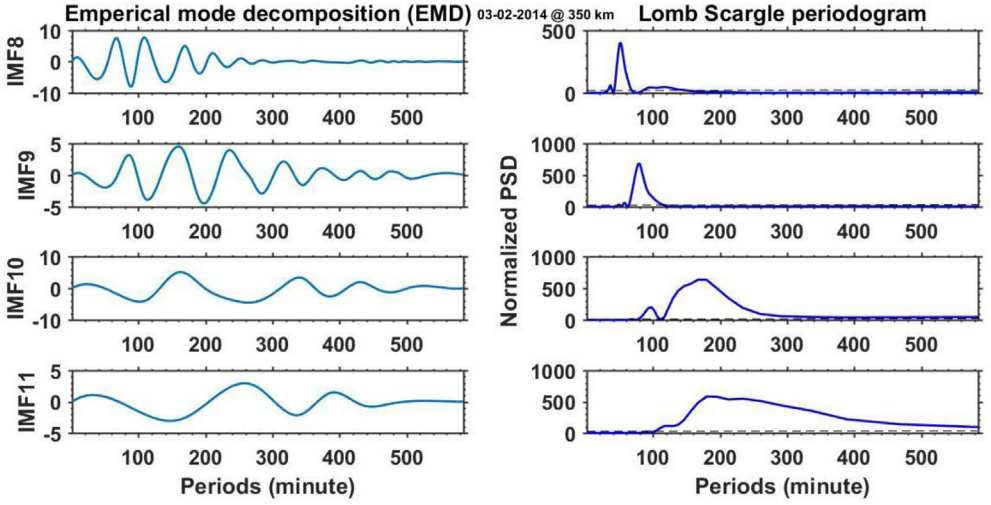

Fig. 5. Left side indicate the Empirical mode decomposition-intrinsic mode frequencies (EMD-IMFs) of OH zenith intensity, 30 MHz radar E-region drift velocity and F-region SNR (at 350 km) on 03 February 2016, and right side shows their respective Lomb-Scargle Periodogram (LSP) with 95% confidence level.

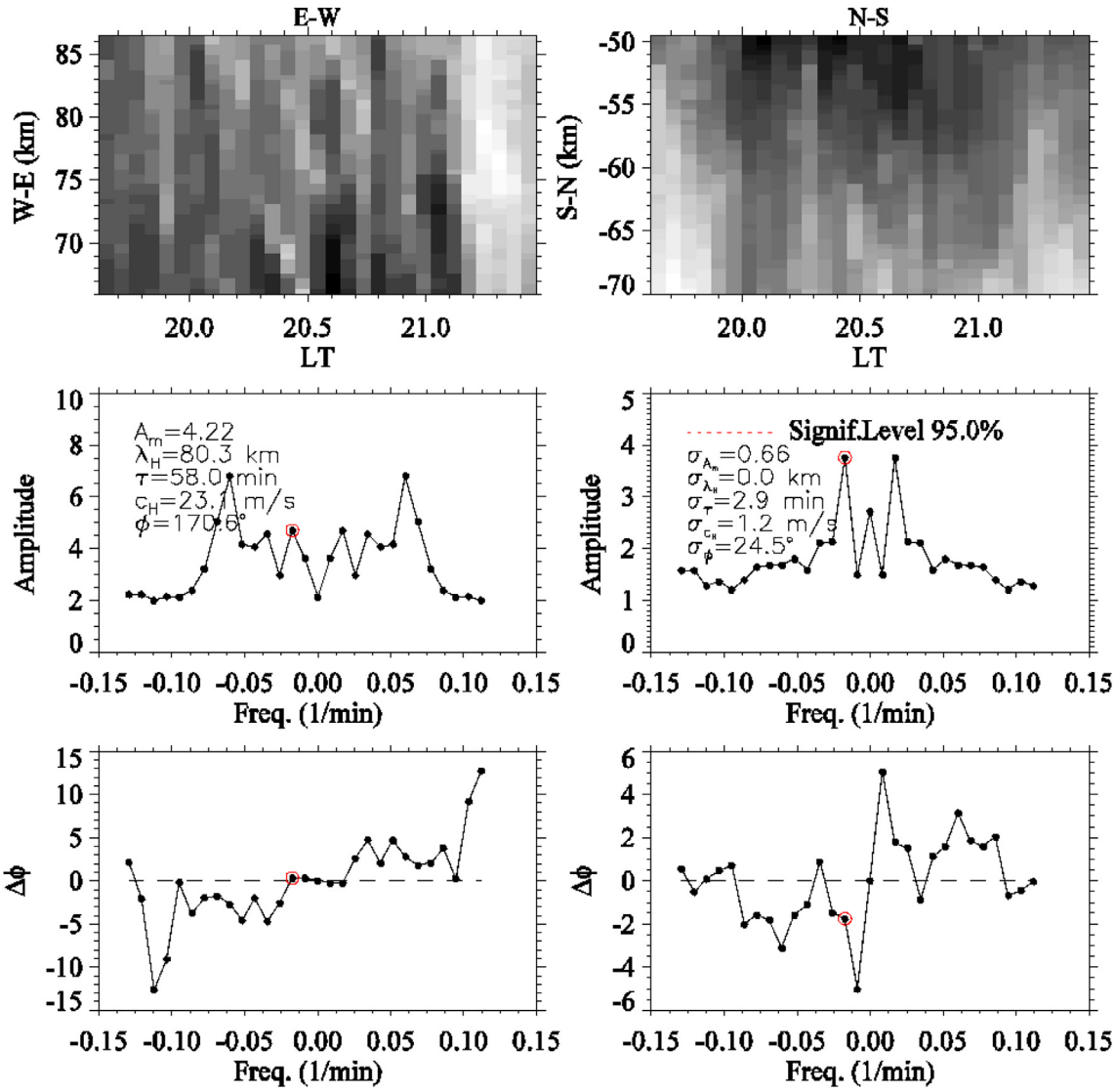

Fig. 6. The keogram analysis of OH airglow emission images on 03 February 2014. Left panels are for the zonal (east-west) keogram and right panels are for meridional (north-south) keogram. The first row shows the zoomed area of the keograms used in the estimation of the gravity wave. Second row show the spectrum (amplitude versus frequency) of the dominant periodicities. Third row display the phase of the periodicity shown in the second row. All periodicities are estimated considering 95% of confidence level.

between them. Their mean is subtracted from the residual data which is called the first component. This processes will be repeated many times whereby the first component treated as data for the second component, similarly the second component act as data for third component, likewise this process will continue till the IMFs exist (i.e. earlier mentioned assumptions will not be satisfied). This is called shifting processes. It has two effects 1) it eliminates the riding waves and 2) smoothing the uneven amplitudes. The detailed description, advantages and disadvantages of this method is detailed by Huang et al. (1998).

To identify the predominant wave periods from the IMFs the LSP analysis is also used in the present study. EMD with LSP analysis of OH zenith intensity, E-region drift velocity and F-region SNR at 350 km is shown in Fig. 5 and the detailed description of this figure is given in later section.

3.2.2. Keogram analysis

To estimate medium frequency gravity wave period in the OH peak emission altitude (~85 km), keogram analysis is used for the OH emission zenith intensity data, because using the Keogram analysis wave period, phase speed, wavelength and horizontal propagation angle can be derived. These parameters are essential for identifying the source of the wave using reverse ray tracing techniques. Thus, in addition to the LSP, Keogram analysis is also used. Fig. 6 shows the keogram of OH airglow emission images on 03 February 2014 (remaining night keograms are not shown here). Left panels are for the zonal (EW) keogram and right panels are for meridional (NS) keogram. The first row shows the zoomed area of the keograms used in the estimation of the gravity wave parameters. Second row displays the spectrum (amplitude versus frequency) of the dominant periodicities. Third row indicates the phase of the periodicity shown in the second row. All periodicities are estimated considering 95% of confidence level. All the derived wave parameters from the keograms are shown in Table 2. Estimation of the medium scale gravity waves is made using the keogram technique, which consist of slices of the airglow images taken in the NS and EW direction (in a temporal sequence). Further details can be found in Paulino et al. (2011) and Figueiredo et al. (2018).

3.2.3. Waves in the MLT region and F-region

To investigate the signatures of gravity waves in the MLT region

Table 2
Medium scale gravity wave (MSGW) parameters deduced from OH keogram analysis.

Sl. No.	Date	Wavelength (km)	Period (min)	Azimuth propagation angle (from north to clockwise direction)	Phase speed (m/s)	Amplitude (%)
1	03-02-2014	50.8 ± 15.9	25.7	98.9	32.9	0.97
		80.3 ± 8.3	58	170.6	23.1	4.22
2	04-02-2014	142.5 ± 38.8	27.7	73.4	85.7	1.28
		165.6 ± 10.6	80	147.8	34.5	6.27
3	05-02-2014	333.2 ± 44.9	41.6	65.2	133.49	7.93
		245.1 ± 20.3	38.7	105.6	37.2	6.17
4	06-02-2014	236.2 ± 24.3	51.5	155.9	76.44	3.62
		505.9 ± 50.5	57.3	128.8	147.1	11.46

Table 3
Predominant wave period from Keogram, EMD and LSP analysis.

Sl. No.	Date	OH Image data wave period (min) (peak emission altitude ~85 km)		30 MHz radar wave period (min) from LSP	
		keogram	LSP	E region (~110 km)	F region (350 km)
1	03-02-2014	25.7, 58	29, 47.3, 57.5, 100	28.5, 51.5, 200	37, 50.78, 77.86
2	04-02-2014	27.7, 80	36, 42, 49, 89, 130	86, 106, 334.3	NIL
3	05-02-2014	41.6, 38.7	56, 70	61, 122, 193	57, 118, 148,
4	06-02-2014	51.5, 57.3	42	79, 94	84, 110, 210

[present case OH emission altitude (~85 km) and E-region (~110 km)] and F-region (350 km); EMD, LSP and Keogram analysis on the E-region drift velocity, F-region SNR, and mesospheric OH airglow emission zenith intensity over Gadanki is performed. Fig. 5 show the various IMFs (left side) and their respective LSP (right side) analysis on 03 February 2014. LSP analysis shows the predominant wave periods with 95% confidence level. Similar kind of analysis is carried out for remaining nights (04, 05, and 06 February 2014) as well (figures are not shown here). In addition, keogram analysis is also performed for the OH images because from which various waves parameters such as period, wavelength, phase propagation angle and phase speed can be extracted (essential for ray tracing technique as detailed in the previous section). Wave parameters derived from the above mentioned methods are presented in Tables 2 and 3. Furthermore, common periodicities observed in the OH emission altitude and E-region are highlighted in red color (see Table 3). Form Tables 2 and 3, one can clearly understand that the wave characteristics are have large day-to-day variations. On 03 February 2014, there are four predominant wave periods in the OH emission altitude with periodicities of 29, 47.5, 57.5 and 100 min, and three predominant waves with period 28.5, 51.5 and 200 min are noted in the E-region drift. Among these, two of them (28.5, 51.5) have almost similar periodicity in both the regions, that are noted in the keogram analysis (25.7 and 58 min) as well. Consequently, it is assumed that these are the same waves which propagate vertically from mesosphere to E-region. Please note here that, based on the background wind condition (Doppler shift) one can expect variation in the intrinsic frequency. Thus, this might be a possible reason for the small differences observed in the wave periods between the OH emission altitude and E-region.

Out of these four nights, common wave periods are noted in the MLT region (i.e. OH emission altitude and E-region) on three nights (03, 04, and 05 February 2014) out of which two nights (03, and 05 February 2014) EPBs are observed in the F-region (OI 630 nm airglow imager data and the 30 MHz radar RTI maps) and there is no depletion on 04 February 2014. Simultaneously, on 06 February 2014 a strong plasma bubble signature is observed in both OI630nm airglow images as well as 30 MHz radar RTI maps, however there was no common wave period in the OH emission altitude and E region during this night. At the same time, E-and F-region show a common wave period on this night.

4. Discussion

Present study shows that there are common wave oscillations present in the mesosphere as well as in the E-region drift velocity data for three nights (03, 04, and 05 February 2014) and no common period waves in the OH emission altitude and E-region during one night (06 February 2014). Based on these, the core problem is organized into three parts as follows.

1) Occurrence of EPBs with mesospheric gravity waves
2) Identifiable mesospheric gravity waves with no EPB occurrence
3) Occurrence of EPBs without mesospheric gravity waves

Here, please note that, though the time series (starting time) of the E region drift and OH imager data are not same but during the data avail duration both data looks almost similar. Therefore, it is presumed that any wave feature present in the pre-midnight E-region might be present in the OH emission altitude as well. Further, all these nights' background ionospheric conditions are comparable (except wind condition) as well as favorable for the generation of EPB because all these nights h′F rises above 350 km and the vertical drift reaches 40 m/s and above. Therefore, the present discussion only focuses on the day-to-day variabilities in the seed perturbation.

4.1. Occurrence of EPBs with mesospheric gravity waves

On 03 February 2014, two waves are noted in OH images keogram analysis, and four wave periods in the OH emission zenith intensity LSP analysis. From Table 2, it can be clear seen that similar kind of wave periods are present in the E-region as well (hereafter we will only discuss about the waves which are noted commonly in the keogram and LSP analysis).

Observed characteristics of these two waves are different, for example, one is propagating in the zonal direction (towards east ~98.7°) with horizontal wavelength and observed period of 50.8 ± 15.9 km and, 25.7 min respectively, and another one is propagating in the meridional direction (towards south ~170°) with horizontal wavelength and observed period of 80.3 ± 8 km and, 58 min respectively. On this night, E-region drift also shows similar periods (28.5 and 51.5, see Table 2). Earlier, using the Rayleigh lidar temperature (70–75 km) data, VHF radar E region drifts Taori et al. (2011) attributed that the common periods could be taken as an evidence for the vertical

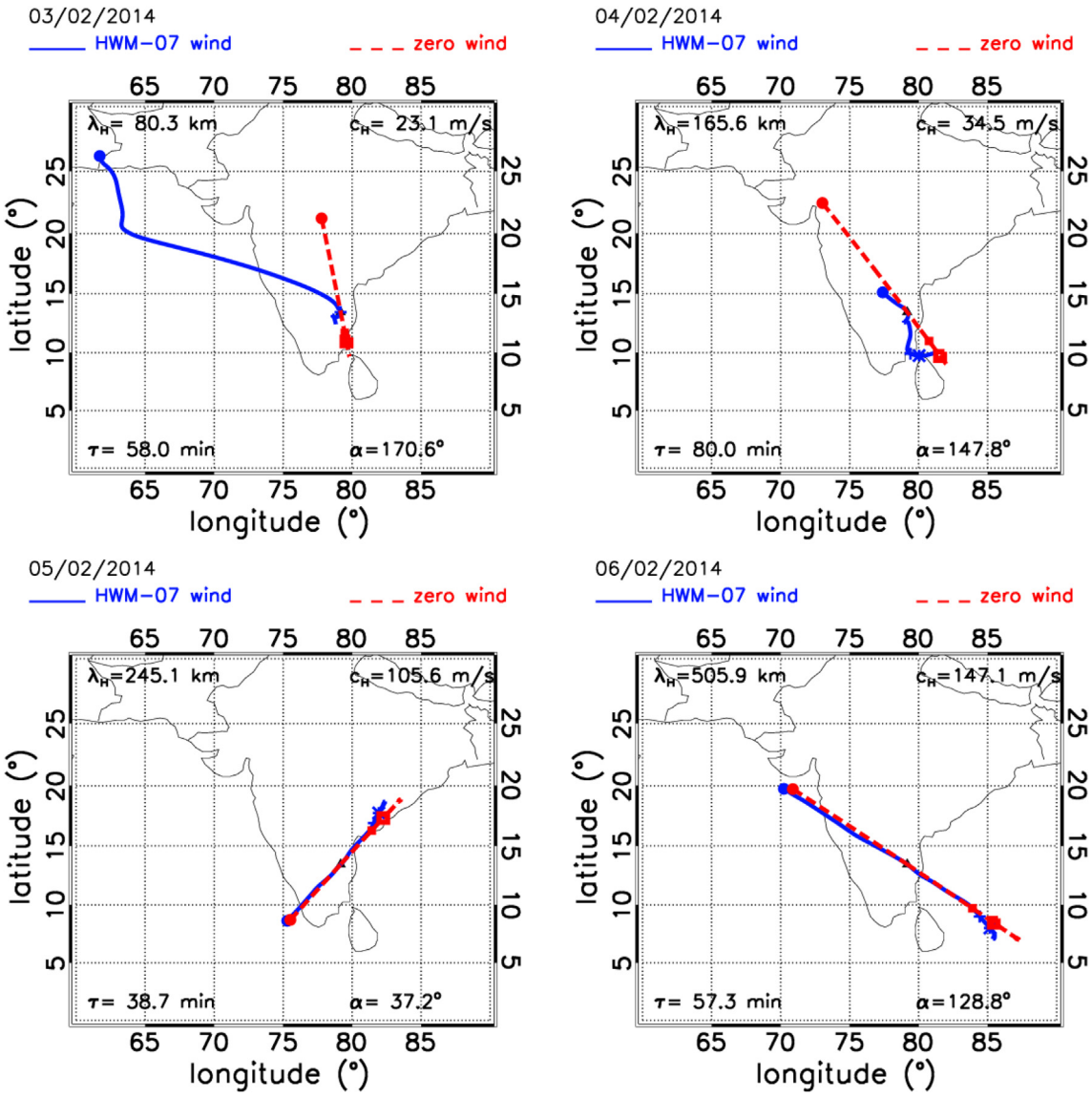

Fig. 7. Ray-tracing results for four of the noted wave events during 03–06 February 2018. Solid blue lines are for the HWM07-model and solid red lines are for zero wind condition. The triangle indicates the location of Gadanki. Filled circles indicate the position/time of the gravity waves on the ground. Plus and filled square symbols indicate where/when the gravity waves have the maximum amplitude into the thermosphere. Star and open square show where/when the gravity waves have less than 1% of their initial amplitude. Horizontal wavelength and phase period are given in right side top and bottom corner respectively. Phase speed and propagation angle of the wave events are given in left side top and bottom corner respectively.

propagation of the waves. To trigger the EPB, wave propagation direction must be perpendicular or nearly perpendicular to the magnetic meridian (Tsunoda, 2010a). Therefore, it is presumed that the wave that is propagate in the zonal direction can be a potential source for triggering the EPB. However, on this night zonally propagating wave amplitude is smaller than the meridionally propagating wave. To understand the link, we have to find whether the observed small amplitude gravity wave is capable enough to trigger the EPB or not? If yes, at which circumstance it might be acted as a potential seed perturbation? To address this questions, evening time E-region condition is checked using the 30 MHz radar RTI map that shows a strong E-region irregularity signature (figure not shown here). Given this situation, the upward propagating gravity wave (even with small amplitude) can generate the polarization electric field effectively that can be mapped into the F-region and seed the EPB.

Previously, Aveiro and Hysell (2010) and Varney et al. (2009) suggested that on top of gravity wave amplitudes and horizontal wavelengths, direction of propagation is also important to generate suitable polarization electric fields. For example, when the wave vector is nearly perpendicular to the magnetic meridian and the vertical wavelength is large, detectable electric field can be created by gravity waves because at this direction the fields are not sorted out by conduction along the magnetic field lines (Varney et al., 2009). Present result show that the observed wave propagates in the zonal direction with an angle of ~98.9° respect to north (clockwise direction from the north as shown in Table 2). In addition, strong evening time E-region irregularities are also noted in the radar backscatter. Therefore, it is presumed that zonally propagating even small amplitude gravity waves also can trigger the EPB when there is a strong irregularity in the evening time E region.

On 05 February 2014, there are two waves in the keogram as well as LSP analysis, conversely, the observed periodicity of these waves are different (see Table 3). E-region drift velocity show three predominant wave periods, among them one of the wave period matches with the LSP wave period. However, the periodicity which are estimated from the keogram analysis and LSP is slightly different from each other.

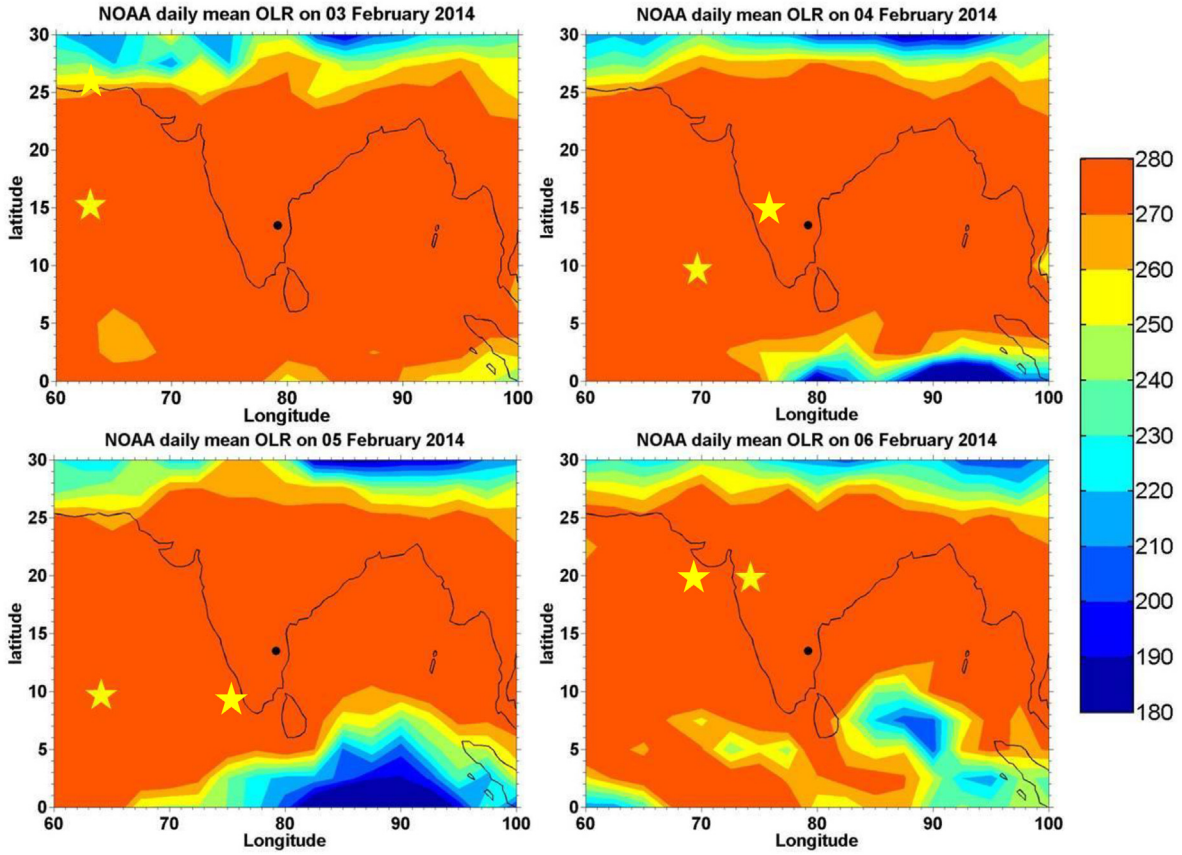

Fig. 8. Daily mean NOAA outgoing long wave radiation (OLR) from 03 February 2014 to 06 February 2014. In these figures, black dot indicates the airglow observation location (i.e. Gadanki). The region with OLR less than 220 W/m^2 indicator of deep convection are considered.

During this night there are weak depletions with inter-depletion distance of ~55.8 ± 5 km and ~376 ± 33 km respectively. The large spatial scale depletion is strikingly nearly same as that of the horizontal wavelength (333.2 ± 44.9 km) of one of the medium scale gravity wave derived from the OH images keogram.

Using three-dimensional time-dependent general circulation model [Coupled Middle Atmosphere-Thermosphere-2 (CMAT2) with their recently developed (Yiğit et al., 2008) spectral nonlinear gravity wave scheme suitable for thermosphere general circulation models (GCMs)] Yiğit and Medvedev (2010) showed direct gravity wave propagation up to thermospheric heights (more than 300 km). Our observation is in basically in agreement with what has been proposed by three-dimensional general circulation models. Because it has been at least about ten years since it was shown "globally" that primary gravity waves from the lower atmosphere penetrate into the thermosphere and reach different heights (Yiğit et al., 2009; Yiğit and Medvedev, 2017). In addition, they also showed that the typical horizontal wavelengths of internal gravity waves observed in the thermosphere usually range between 100 and 500 km. Furthermore, earlier observational studies show that waves with horizontal wavelength more than 100 km are suitable candidate for directly propagating to the bottom of the F-layer (Kelley et al., 1981; Takahashi et al., 2009; Taori et al., 2011a,b; Paulino et al., 2011). Using multiple ground based observations Narayanan et al. (2012) reported that coexistence of large scale wave like structure (LSWS) with small scale wave structures (SSWS) are potential candidates for triggering the EPB. The present case, two different size inter depletion distances show the possibility of presence of LSWS and SSWS in the bottom of the F layer, furthermore the LSWS wavelength is comparable to the mesospheric gravity wave. Therefore, it is presumed that during this night the wave that is noted in the mesospheric OH emission altitude may be directly penetrating into the bottom of the F-layer that triggered the EPB.

4.2. Identifiable mesospheric gravity waves with no EPB occurrence

Two wave periods with different parameters in keogram analysis (see Table 2) and five waves from the LSP analysis are noted on 04 February 2014. There is a common period wave in both the OH emission altitude (80 and 89 min) and E-region (86 min). From the keogram analysis, it is identified that one propagates towards northeast and another one towards southeast. On this day h′F rises up to 410 km after sunset. However, there is no EPB occurrence observed conversely only very weak back scattered signals are noted in 30 MHz radar at around 22:30 IST (17:00UTC). Period of the wave is about 80/89 min which is higher than the earlier night (03 February, 26 min). Furthermore, propagation angle and horizontal wavelength are 147.8° and 165.6 ± 10.6 km compared to about 98.9° and ~51 km on 03 February 2014 respectively. These differences can be seen in Table 2. Though the background conditions (h′F value is ~410 km, during sunset period vertical drift goes up to 40 m/s and wave amplitude also greater than previous day) on this night is favorable for the occurrence of EBP. This discrepancy might happen due to the variation in gravity wave phase front alignment with magnetic field lines. As discussed by Tsunoda (2010b) that if plane wave phase front is not aligned with the magnetic field, then the net polarization electric field which are generated by these waves will disappear. However, for circular gravity waves, modulation in the polarization electric field is effective up to ~40° from the zonal direction (Krall et al., 2013). Therefore, there is possibility that the noted wave might be a plane wave rather than circular wave. In addition, there is another possibility that during this night transequatorial thermospheric wind might enhanced which might be inhibit/suppress the growth of the EPB as described by Abdu et al.

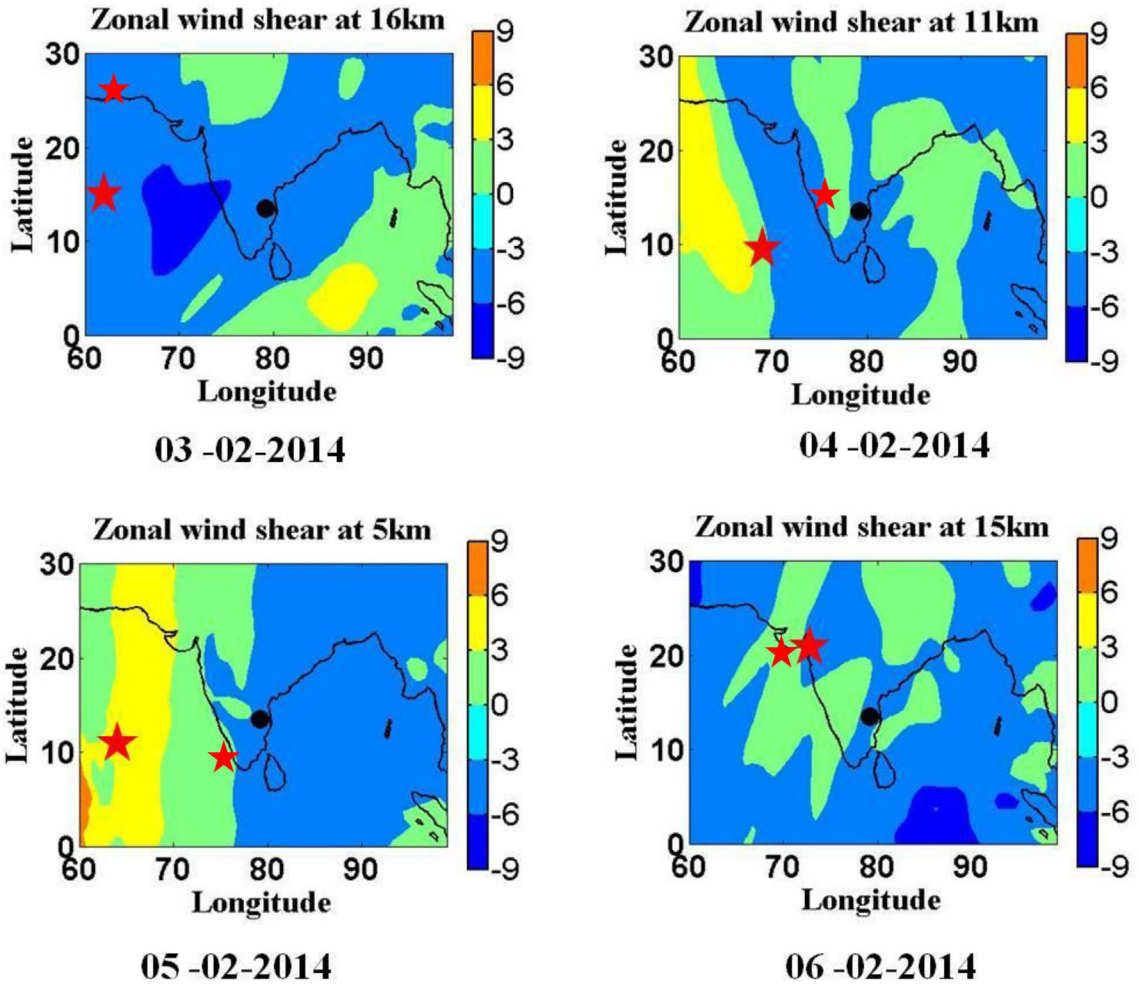

Fig. 9. Six-hour mean ECMWF interim reanalysis (ERA) zonal wind shear for 03–06 February 2014 where the wind shear maximum at ray termination region. In these figures black dot denotes the airglow observation location (i.e., Gadanki) and the red star indicates the ray termination region with wind condition.

(2009). Additionally, there appears to be present a connection between the intensity of the PRE vertical drift and the amplitude and phase of the precursor oscillations, with implications on a possible tidal gravity wave interaction modifying the winds in evening E-layer, and thereby, modifying also the PRE development. Further, the PRE vertical drift, when weakly developed, can be suppressed or even reversed to downward by upward propagating gravity waves of large enough intensity. In this way, the gravity waves activity may even lead to suppression of the post-sunset ESF/EPB development (e.g., Abdu, 2019). However, on this night the vertical drift reaches up to 40 m/s. Therefore, at this point we are not sure which factor inhibited the generation of EPB during this night. Thus, it need to be studied further with background wind information. Please note that, during this night there is no irregularities observed in the E-region.

4.3. Occurrence of EPBs without mesospheric gravity waves

On 06 February 2014 the plasma depletion is very strong compared to the 05 February 2014. However, OH emission altitude and E-region does not show any common wave period oscillations (though there are four wave events). Conversely, during this night base of the F-layer is rises about 475 km [the highest among the cases considered (see Fig. 4)]. There can be two possibilities that might triggered the EPB on this day 1) collisional shear instability that occurs in the bottom of the F-layer (Hysell and Kudeki, 2004) or 2) post sunset equatorial eastward thermospheric wind may also initiate the observed EPB (Kudeki et al., 2007). In addition, irrespective of the MLT region gravity wave, thermospheric origin gravity wave also can play possible role in the generation mechanism. However, with existing data set drawing a solid conclusion is difficult for this night as it should be studied with thermospheric wind measurements.

4.4. Identification of gravity wave sources and dissipation region

Some of the earlier model simulation studies show the vertical propagation of gravity waves from the troposphere to thermosphere (Horinouchi et al., 2002; Miyoshi et al., 2014; Vadas and Fritts, 2005, 2004; Miyoshi and Fujiwara, 2008; Yiğit et al., 2008; Yiğit and Medvedev, 2010). For example, to study the vertical propagation of the sub-grid (small) scale gravity waves from the troposphere to the ionosphere Yiğit et al. (2008) have implemented the extended parameterization into the Coupled Middle Atmosphere and Thermosphere-2 GCM (CMAT2) model, and simulated to have a global view of the small-scale gravity wave propagation into the thermosphere. Recent review articles by Yiğit et al. (2016) and Yiğit and Medvedev (2015 and reference therein) provides an extensive overview of vertical coupling by gravity waves from the lower atmosphere into thermosphere during sudden stratospheric warming (SSW) condition and non SSW condition. Over all, these studies are primarily confined on the vertical propagation characteristics of the gravity waves, their various dissipation mechanism and their impact in the thermosphere (i.e. heating/cooling of the thermosphere).

In this section, using reverse and forward ray tracing technique we provide a detailed discussion about the waves noted in the OH airglow

emission altitude (i.e. mesosphere), where they are coming from (i.e. sources for the observed gravity waves)? and how far they can propagate in the vertical direction? Earlier reports suggest that these waves are generated/originated due to lower atmospheric phenomena such as deep convection, jet streams, orography and geostropic adjustments etc., (Pfister et al., 1993; Nishioka et al., 2013; Plougonven and Zhang, 2013; Sivakandan et al., 2016). Therefore, to identify the sources of the observed gravity waves, reverse ray tracing analysis is carried out and forward ray tracing analysis also performed to ascertain whether the waves could reach the ionospheric/thermospheric altitudes.

During these four nights (from 03 February 2014 to 06 February 2014), over all, eight gravity wave events are noted in the OH image keograms. For these waves reverse and forward ray tracing analysis is carried out andthe results are shown in Fig. 7 (only 4 wave events ray tracing results are shown here). In these figures solid blue lines corresponds to the wind inputs using HWM07-model and solid red lines represent zero wind condition. The triangles indicate the observation location (i.e. Gadanki). Filled circles indicate the position/time of the gravity waves on the ground. Plus and filled square symbols indicate where/when the gravity waves have the maximum amplitude into the mesosphere and thermosphere. Star and open squares show where/when the gravity waves have less than 1% of their initial amplitude. Horizontal wavelength and phase period are given in right side top and bottom corner, respectively. Phase speed and propagation angle of these wave events are given in left side top and bottom corner, respectively. Note that whether it is with or without wind condition, most of the times the ray path is somewhat similar but the terminating points differ indicating that the background wind affects the gravity wave propagation. Forward ray tracing results show that out of eight wave events, two waves dissipated below the turbopause (~110 km) and remaining six waves propagate up to the altitude of about 130–200 km (figures not shown here). Furthermore, reverse ray tracing results show that all these wave events are of tropospheric origin (though there may be uncertainty in the model wind). Gravity wave generation occurs in the lower atmosphere by wide range of sources such as mountains, hills (orographic sources), convection, jet streams, wind shear, geostrophic adjustment (non-orographic sources), etc. It is presumed that among all the above mentioned sources, deep convection is a plausible source of generation of gravity waves in the equatorial and low latitude region (Nakamura, 2003). Recently, using three years of spring equinox months (March and April) airglow imager data and NOAA outgoing longwave radiation (OLR) data Sivakandan et al. (2016) reported that over the Indian low latitudes ~66% gravity waves are generated by tropospheric deep convection.

In this aspect to identify the source mechanism, the ray terminating points are compared with daily mean NOAA OLR data. The region where the OLR value less than 220 W/m^2 are considered as an indicator of deep convection. Fig. 8, shows the daily mean NOAA OLR from 03 February 2014 to 06 February 2014. In these, figures X-axis denotes the longitude, Y-axis denotes the latitude, black dot indicates the airglow observation location (i.e. Gadanki) and the yellow star indicates the source region with wind condition. While comparing with the source region (reverse ray tracing terminating point) and the OLR values, it is observed that out of these eight events, seven events are not terminating to the convection regions. However, on 03 February a wave event terminates nearby the convective region. As the spatial (2.5° × 2.5° latitude and longitude) and temporal resolution (daily mean) of the NOAA OLR is very poor, thus it can be said that this wave may be triggered by the tropospheric deep convection. This result shows that during these days' majority of the waves are not generated by the convective activity. Recently, Pramitha et al. (2015) reported that wind shears also could be a possible source for generation of gravity waves in the low latitude region.

An attempt is made to understand the source of observed wave features by wind shear using ECMWF interim reanalysis (ERA) data. Vertical shears of the horizontal (zonal and meridional) wind is calculated in the height range of 1–21 km. Fig. 9 show the six-hourly mean ECMWF interim reanalysis (ERA) zonal wind shear for 03–06 February 2014 where the wind shear is maximum at source region (ray terminating region) (actually the wind shear is calculated for all the height from 1 km to 22 km, however, the figure in display here only shows where the shear is more in the ray path). In these figures, black dot denotes the airglow observation location (i.e., Gadanki) and the red star indicates the source region with wind condition. Prior to the gravity wave generation by wind shear, the atmosphere should be unstable and the wind shear must exceed 2N (N is the buoyancy frequency) (Bühler and McIntyre, 1999; Fritts and Rastogi, 1985, Scinocca and Ford, 2000). However, the wind shear noted on these days are weak so it could not make the atmosphere unstable at the ray path. However, except 03 February 2014 remaining all days where the ray terminates around that region, wind shear shows the directional changes. This kind of situation can make the background atmosphere become unstable (though the shear is comparatively less) Thus, it is assumed that for those wave events, wind shear might be a plausible source. Therefore, from the present results, it is presumed that the observed mesospheric gravity waves (noted in the OH airglow images) are generated in the troposphere by wind shear (mostly) and convection. Furthermore, some of the upward propagating waves are get dissipated around or below the turbopause and the remaining waves propagate up to about 130–200 km.

5. Summary and conclusions

Using four consecutive nights (03–06 February 2014) of multi instruments (all sky airglow imager, 30 MHz radar, and ionosonde) data set, the generation mechanism of EPBs and the role of gravity waves in seeding of the R-T instability during quiet geomagnetic conditions is studied. Together with the observations; reverse and forward ray tracing techniques are also used to investigate the origin and dissipation region of the gravity wave events. Furthermore, to identify the source of the observed wave events NOAA-OLR and vertical shear of the horizontal wind around the reverse ray termination points are checked. The results obtained from the present investigations are summarized as follows:

1. Out of four days, during three days the F-region plasma depletion in OI630 nm airglow emission as well as the 30 MHz radar SNR signal is noted that are supported by the ionosonde h′F values.
2. Keogram as well as the EMD-LSP analysis exhibit the presence of medium scale gravity waves in all these four nights with day to day varying wave parameters. Most of these noted waves are found to propagating toward east (except in one case).
3. On 3 February 2014 it is noted that zonally propagating gravity wave with small amplitude also can trigger the EPB when there is a strong irregularity existing in the Eregion.
4. On 04 February 2014, the F layer height, wave amplitude and the wave propagation angle are suitable for EPB seeding. However, there was no plasma bubble on this night. It indicates that together with sinusoidal perturbations; vertical shear, thermospheric eastward wind and transequatorial wind also may play a role on the plasma bubbles generation. It needs to be studied further for better understanding.
5. Reverse ray tracing results suggest that these waves are generated in the lower atmosphere and forward ray tracing results show that they can propagate vertically up to ~130–200 km.
6. NOAA daily mean OLR and the ECMWF vertical shear of the horizontal wind suggest that out of these eight wave events one might be generated by the tropospheric convection, wind shear might be a possible source for other six waves and for remaining one wave, the source is neither convection nor wind shear. However, it need to be verified with observational wind data.

Acknowledgement

The author thanks the Director NARL for support and encouragement. We thank Prof. D.C. Fritts for his fruitful discussions about the generation of gravity waves by wind shear. We thank NARL airglow team members Dr. Kamalakar, Liyakat Basha and HF radar team members for carrying out night observations. M. Sivakandan thank Dr. D. Selvaraj, Dr. Pavan Chaitanya and Dr. Priyanka Ghosh for their support. We thank Ms. C. A. Smith of NOAA Earth System Research Laboratory for providing the interpolated OLR data (Source: www.esrl.noaa.gov/psd/data/gridded/data.interp_OLR.html). ECMWF interim reanalysis (ERA) data is downloaded from http://apps.ecmwf.int/datasets/data/interim-full-daily/levtype=pl/. I. Paulino thanks to the Conselho Nacional de Desenvolvimento Científico e Tecnológico (CNPq - 303511/2017–6) for the financial support.

Appendix A. Supplementary data

Supplementary data related to this article can be found at https://doi.org/10.1016/j.jastp.2019.04.006.

References

Abdu, M.A., 2019. Day-to-day and short-term variabilities in the equatorial plasma bubble/spread F irregularity seeding and development. Prog. Earth Planet. Sci. 6, 1–22. https://doi.org/10.1186/s40645-019-0258-1.

Abdu, M.A., Batista, I.S., Reinisch, B.W., De Souza, J.R., Sobral, J.H.A., Pedersen, T.R., et al., 2009. Conjugate Point Equatorial Experiment (COPEX) campaign in Brazil: electrodynamics highlights on spread F development conditions and day-to-day variability. J. Geophys. Res.: Space Physics 114 (4). https://doi.org/10.1029/2008JA013749.

Aveiro, H.C., Hysell, D.L., 2010. Three-dimensional numerical simulation of equatorial F region plasma irregularities with bottomside shear flow. J. Geophys. Res.: Space Physics 115 (11), 1–14. https://doi.org/10.1029/2010JA015602.

Brasseur, G.P., Solomon, S., 2005. Aeronomy of the Middle Atmosphere, vol. 32 atmospheric and oceanographic sciences library.

Bühler, O., McIntyre, M.E., 1999. On Shear-Generated Gravity Waves that Reach the Mesosphere. Part II: Wave Propagation. Journal of the Atmospheric Sciences 56, 3764–3773. https://doi.org/10.1175/1520-0469(1999)056%3e3764:OSGGWT%3c2.0.CO2.

Costa, E., Kelley, M.C., 1978. On the role of steepened structures and drift waves in equatorial spread F. J. Geophys. Res. 83 (A9), 4359. https://doi.org/10.1029/JA083iA09p04359.

Drob, D.P., Emmert, J.T., Crowley, G., Picone, J.M., Shepherd, G.G., Skinner, W., et al., 2008. An empirical model of the Earth's horizontal wind fields: HWM07. J. Geophys. Res.: Space Physics 113 (12), 1–18. https://doi.org/10.1029/2008JA013668.

Dungey, J.W., 1956. The influence of the geomagnetic field on turbulence in the ionosphere. J. Atmos. Terr. Phys. 8 (1), 39–42. https://doi.org/doi.org/10.1016/0021-9169(56)90089-7.

Fejer, B.G., Scherliess, L., de P., E.R., de Paula, E.R., 1999. Effects of the vertical plasma drift velocity on the generation and evolution of equatorial spread F. J. Geophys. Res.: Space Physics 104 (A9), 19859–19869. https://doi.org/10.1029/1999JA900271.

Figueiredo, C.A.O.B., Takahashi, H., Wrasse, C.M., Otsuka, Y., Shiokawa, K., Barros, D., 2018. Medium-scale traveling ionospheric disturbances observed by detrended total electron content maps over Brazil. J. Geophys. Res.: Space Physics 123, 2215–2227. https://doi.org/10.1002/2017JA025021.

Fritts, D.C., Rastogi, P.K., 1985. Convective and dynamical instabilities due to gravity-wave motions in the lower and middle atmosphere - theory and observations. Radio Sci. 20 (6), 1247–1277.

Fritts, D.C., Abdu, M.A., Batista, B.R., Batista, I.S., Batista, P.P., Buriti, R., et al., 2009. Overview and summary of the spread F experiment (SpreadFEx). Ann. Geophys. 27 (5), 2141–2155. https://doi.org/10.5194/angeo-27-2141-2009.

Horinouchi, T., Nakamura, T., Kosaka, J. ichi, 2002. Convectively generated mesoscale gravity waves simulated throughout the middle atmosphere. Geophys. Res. Lett. 29, 10–13. https://doi.org/10.1029/2002GL016069.

Huang, J., MacDougall, J.W., 2005. Legendre coding for digital ionosondes. Radio Sci. 40 (4), 1–11. https://doi.org/10.1029/2004RS003123.

Huang, N., Shen, Z., Long, S., Wu, M., Shih, H., Zheng, Q., et al., 1998. The empirical mode decomposition and the Hilbert spectrum for nonlinear and non-stationary time series analysis. Proc. Math. Phys. Eng. Sci. 454 (1971) 995, 903. https://doi.org/10.1098/rspa.1998.0193.

Hysell, D.L., Kudeki, E., 2004. Collisional shear instability in the equatorial F region ionosphere. J. Geophys. Res.: Space Physics 109 (A11), 1–8. https://doi.org/10.1029/2004JA010636.

Hysell, D.L., Kelley, M.C., Swartz, W.E., Woodman, R.F., 1990. Seeding and layering of equatorial spread F by gravity waves. J. Geophys. Res. 95 (A10), 17253. https://doi.org/10.1029/JA095iA10p17253.

Jayachandran, B., Balan, N., Rao, P.B., Sastri, J.H., Bailey, G.J., 1993. HF Doppler and Ionosonde observations on the onset conditions of equatorial spread F. J. Geophys. Res. 98750 (1) 741–13.

Kelley, M.C., Larsen, M.F., LaHoz, C., McClure, J.P., 1981. Gravity wave initiation of equatorial spread F: A case study. J. Geophys. Res. 86 (A11), 9087. https://doi.org/10.1029/JA086iA11p09087.

Khomich, V.Y., Semenov, A.I., Shefov, N.N., 2008. Airglow as an indicator of upper atmospheric structure and dynamics. Airglow as an Indicator of Upper Atmospheric Structure and Dynamics. . https://doi.org/10.1007/978-3-540-75833-4.

Kishore, P., Velicogna, I., Venkat Ratnam, M., Jiang, J.H., Madhavi, G.N., 2012. Planetary waves in the upper stratosphere and lower mesosphere during 2009 Arctic major stratospheric warming. Ann. Geophys. 30 (10), 1529–1538. https://doi.org/10.5194/angeo-30-1529-2012.

Krall, J., Huba, J.D., Joyce, G., Hei, M., 2013. Simulation of the seeding of equatorial spread F by circular gravity waves. Geophys. Res. Lett. 40 (1), 1–5. https://doi.org/10.1029/2012GL054022.

Kudeki, E., Akgiray, A., Milla, M., Chau, J.L., Hysell, D.L., 2007. Equatorial spread-F initiation: post-sunset vortex, thermospheric winds, gravity waves. J. Atmos. Sol. Terr. Phys. 69 (17–18), 2416–2427. https://doi.org/10.1016/j.jastp.2007.04.012.

Lighthill, J., 1978. Waves in Fluids. Cambridge University Press, New York.

Manju, G., Devasia, C.V., Sridharan, R., 2007. On the seasonal variations of the threshold height for the occurrence of equatorial spread F during solar minimum and maximum years. Ann. Geophys. 25, 855–861. https://doi.org/10.5194/angeo-25-855-2007.

Marks, C.J., Eckermann, S.D., 1995. A three-dimensional nonhydrostatic ray-tracing model for gravity waves: formulation and preliminary results for the middle atmosphere. J. Atmos. Sci. 2. https://doi.org/10.1175/1520-0469(1995)052%3e1959:ATDNRT%3c2.0.CO.

McClure, J.P., Hanson, W.B., Hoffman, J.H., 1977. Plasma bubbles and irregularities in the equatorial ionosphere. J. Geophys. Res. 82 (19), 2650–2656. https://doi.org/10.1029/JA082i019p02650.

Medvedev, A.S., Yiğit, E., Hartogh, P., 2017. Ion friction and quantification of the geomagnetic influence on gravity wave propagation and dissipation in the thermosphere-ionosphere. J. Geophys. Res. Sp. Phys. 122, 12464–12475. https://doi.org/10.1002/2017JA024785.

Mendillo, M., Baumgardner, J., Pi, X., Sultan, P.J., Tsunoda, R., 1992. Onset conditions for equatorial spread F. J. Geophys. Res. 97 (A9), 13865–13876. https://doi.org/10.1029/92ja00647.

Miyoshi, and Fujiwara, 2008. Gravity waves in the thermosphere simulated by a general circulation model. J. Geophys. Res. 113, 1–11. https://doi.org/10.1029/2007JD008874.

Miyoshi, Y., Fujiwara, H., Jin, H., Shinagawa, H., 2014. A global view of gravity waves in the thermosphere simulated by a general circulation model. J. Geophys. Res. Sp. Phys. 119, 5807–5820. https://doi.org/10.1002/2014JA019848.

Nakamura, T., 2003. Mesospheric gravity waves over a tropical convective region observed by OH airglow imaging in Indonesia. Geophys. Res. Lett. 30 (17), 1999–2002. https://doi.org/10.1029/2003GL017619.

Narayanan, V.L., Taori, A., Patra, A.K., Emperumal, K., Gurubaran, S., 2012. On the importance of wave-like structures in the occurrence of equatorial plasma bubbles: a case study. J. Geophys. Res. Sp. Phys. 116, 1–8. https://doi.org/10.1029/2011JA017054.

Nishioka, M., Tsugawa, T., Kubota, M., Ishii, M., 2013. Concentric waves and short-period oscillations observed in the ionosphere after the 2013 Moore EF5 tornado. Geophys. Res. Lett. 40 (21), 5581–5586. https://doi.org/10.1002/2013GL057963.

Patra, A.K., Taori, A., Chaitanya, P.P., Sripathi, S., 2013. Direct detection of wavelike spatial structure at the bottom of the F region and its role on the formation of equatorial plasma bubble. J. Geophys. Res.: Space Physics 118 (3), 1196–1202. https://doi.org/10.1002/jgra.50148.

Patra, A.K., Srinivasulu, P., Chaitanya, P.P., Rao, M.D., Jayaraman, A., 2014. First results on low-latitude e and F region irregularities obtained using the Gadanki Ionospheric Radar Interferometer. J. Geophys. Res. A Space Phys. 119 (12), 10276–10293.

Paulino, I., Takahashi, H., Medeiros, A.F., Wrasse, C.M., Buriti, R.A., Sobral, J.H.A., Gobbi, D., 2011. Mesospheric gravity waves and ionospheric plasma bubbles observed during the COPEX campaign. J. Atmos. Sol. Terr. Phys. 73 (11–12), 1575–1580. https://doi.org/10.1016/j.jastp.2010.12.004.

Paulino, I., Takahashi, H., Vadas, S.L., Wrasse, C.M., Sobral, J.H.A., Medeiros, A.F., et al., 2012. Forward ray-tracing for medium-scale gravity waves observed during the COPEX campaign. J. Atmos. Sol. Terr. Phys. 90–91 (1), 117–123. https://doi.org/10.1016/j.jastp.2012.08.006.

Pfister, L., Chan, K.R., Bui, T.P., Bowen, S., Legg, M., Gary, B., et al., 1993. Gravity waves generated by a tropical cyclone during the STEP tropical field program - a case study. J. Geophys. Res. 98 (D5), 8611–8638. https://doi.org/10.1029/92JD01679.

Picone, J.M., Hedin, A.E., Drob, D.P., Aikin, A.C., 2002. NRLMSISE-00 empirical model of the atmosphere: statistical comparisons and scientific issues. J. Geophys. Res.: Space Physics 107 (A12), 1–16. https://doi.org/10.1029/2002JA009430.

Plougonven, R., Zhang, F., 2013. Internal gravity waves from atmospheric fronts and jets. Rev. Geophys.(2012). https://doi.org/10.1002/2012RG000419.

Prakash, S., Pandey, R., 1985. Generation of electric fields due to the gravity wave winds and their transmission to other ionospheric regions. J. Atmos. Terr. Phys. 47 (4), 363–374. https://doi.org/https://doi.org/10.1016/0021-9169(85)90016-9.

Pramitha, M., Venkat Ratnam, M., Taori, A., Krishna Murthy, B.V., Pallamraju, D., Vijaya Bhaskar Rao, S., 2015. Evidence for tropospheric wind shear excitation of high-phase-speed gravity waves reaching the mesosphere using the ray-tracing technique. Atmos. Chem. Phys. 15 (5), 2709–2721. https://doi.org/10.5194/acp-15-2709-2015.

Scinocca, J.F., Ford, R., 2000. The nonlinear forcing of large-scale internal gravity waves by stratified shear instability. J. Atmos. Sci. 57 (5), 653–672. https://doi.org/10.1175/1520-0469(2000)057%3e0653:TNFOLS%3c2.0.CO;2.

Singh, S., Johnson, F.S., Power, R.A., 1997. Gravity wave seeding of equatorial plasma bubbles. J. Geophys. Res. 102 (96), 7399–7410.

Sivakandan, M., Paulino, I., Taori, A., Niranjan, K., 2016. Mesospheric gravity wave characteristics and identification of their sources around spring equinox over Indian low latitudes. Atmospheric Measurement Techniques 9 (1), 93–102. https://doi.org/10.5194/amt-9-93-2016.

Takahashi, H., Taylor, M.J., Pautet, P.D., Medeiros, A.F., Gobbi, D., Wrasse, C.M., et al., 2009. Simultaneous observation of ionospheric plasma bubbles and mesospheric gravity waves during the SpreadFEx campaign. Ann. Geophys. 27 (4), 1477–1487. https://doi.org/10.5194/angeo-27-1477-2009.

Taori, A., Sindhya, A., 2014. Measurements of equatorial plasma depletion velocity using 630 nm airglow imaging over a low-latitude Indian station. J. Geophys. Res.: Space Physics 119 (1), 396–401. https://doi.org/10.1002/2013JA019465.

Taori, A., Makela, J.J., Taylor, M., 2010. Mesospheric wave signatures and equatorial plasma bubbles: a case study. J. Geophys. Res.: Space Physics 115 (6), 1–9. https://doi.org/10.1029/2009JA015088.

Taori, A., Dashora, N., Raghunath, K., Russell, J.M., Mlynczak, M.G., 2011a. Simultaneous mesosphere-thermosphere-ionosphere parameter measurements over Gadanki (13.5°N, 79.2°E): first results. J. Geophys. Res.: Space Physics 116 (7), 1–10. https://doi.org/10.1029/2010JA016154.

Taori, A., Patra, A.K., Joshi, L.M., 2011b. Gravity wave seeding of equatorial plasma bubbles: an investigation with simultaneous F region, e region, and middle atmospheric measurements. J. Geophys. Res. Sp. Phys. 116, 1–7. https://doi.org/10.1029/2010JA016229.

Taori, A., Kamalakar, V., Joshi, L.M., Sripathi, S., Patra, A.K., 2012. On the linkage between mesospheric gravity waves and occurrence of equatorial plasma bubble observed during the low solar activity. Indian J. Radio Space Phys. 41 (2), 264–270.

Taori, A., Jayaraman, A., Kamalakar, V., 2013. Imaging of mesosphere-thermosphere airglow emissions over Gadanki (13.5°N, 79.2°E) - first results. J. Atmos. Sol. Terr. Phys. 93, 21–28. https://doi.org/10.1016/j.jastp.2012.11.007.

Tsunoda, R.T., 1985. Control of the seasonal and longitudinal occurrence of equatorial scintillations by the longitudinal gradient in integrated Eregion Pedersen conductivity. J. Geophys. Res. 90 (A1), 447–456. https://doi.org/10.1029/JA090iA01p00447.

Tsunoda, R.T., 2010a. On equatorial spread F: establishing a seeding hypothesis. J. Geophys. Res.: Space Physics 115 (12), 1–9. https://doi.org/10.1029/2010JA015564.

Tsunoda, R.T., 2010b. On seeding equatorial spread F: circular gravity waves. Geophys. Res. Lett. 37 (10), 1–5. https://doi.org/10.1029/2010GL043422.

Vadas, S.L., Fritts, D.C., 2004. Thermospheric responses to gravity waves arising from mesoscale convective complexes. J. Atmos. Sol. Terr. Phys. 66, 781–804. https://doi.org/10.1016/j.jastp.2004.01.025.

Vadas, S.L., Fritts, D.C., 2005. Thermospheric responses to gravity waves: influences of increasing viscosity and thermal diffusivity. J. Geophys. Res. D Atmos. 110 (15), 1–16. https://doi.org/10.1029/2004JD005574.

Vadas, S.L., Fritts, D.C., 2009. Reconstruction of the gravity wave field from convective plumes via ray tracing. Ann. Geophys. 27 (1), 147–177. https://doi.org/10.5194/angeo-27-147-2009.

Vadas, S.L., Taylor, M.J., Pautet, P.D., Stamus, P.A., Fritts, D.C., Liu, H.L., et al., 2009. Convection: the likely source of the medium-scale gravity waves observed in the OH airglow layer near Brasilia, Brazil, during the SpreadFEx campaign. Ann. Geophys. 27 (1), 231–259. https://doi.org/10.5194/angeo-27-231-2009.

Varney, R.H., Kelley, M.C., Kudeki, E., 2009. Observations of electric fields associated with internal gravity waves. J. Geophys. Res. 114 (A2), A02304. https://doi.org/10.1029/2008JA013733.

Weber, E.J., Buchau, J., Eather, R.H., Mende, S.B., 1978. North-south aligned equatorial airglow depletions. J. Geophys. Res. 83 (7), 712. https://doi.org/10.1029/JA083iA02p00712.

Yiğit, E., Medvedev, A.S., 2010. Internal gravity waves in the thermosphere during low and high solar activity: simulation study. J. Geophys. Res. Sp. Phys. 115, 1–16. https://doi.org/10.1029/2009JA015106.

Yiğit, E., Medvedev, A.S., 2015. Internal wave coupling processes in Earth's atmosphere. Adv. Space Res. 55, 983–1003. https://doi.org/10.1016/j.asr.2014.11.020.

Yiğit, E., Medvedev, A.S., 2017. Influence of parameterized small-scale gravity waves on the migrating diurnal tide in Earth's thermosphere. J. Geophys. Res. Sp. Phys. 122, 4846–4864. https://doi.org/10.1002/2017JA024089.

Yiğit, E., Koucká Knížová, P., Georgieva, K., Ward, W., 2016. A review of vertical coupling in the Atmosphere-Ionosphere system: effects of waves, sudden stratospheric warmings, space weather, and of solar activity. J. Atmos. Sol. Terr. Phys. 141, 1–12. https://doi.org/10.1016/j.jastp.2016.02.011.

Yiğit, E., Aylward, A.D., Medvedev, A.S., 2008. Parameterization of the effects of vertically propagating gravity waves for thermosphere general circulation models: sensitivity study. J. Geophys. Res. Atmos. 113, 1–15. https://doi.org/10.1029/2008JD010135.

Yiğit, E., Medvedev, A.S., Aylward, A.D., Hartogh, P., Harris, M.J., 2009. Modeling the effects of gravity wave momentum deposition on the general circulation above the turbopause. J. Geophys. Res. Atmos. 114, 1–14. https://doi.org/10.1029/2008JD011132.